Supplementary Materials for

A hydrated crystalline calcium carbonate phase: Calcium carbonate hemihydrate

Zhaoyong Zou, Wouter J. E. M. Habraken, Galina Matveeva, Anders C. S. Jensen, Luca Bertinetti, Matthew A. Hood, Chang-yu Sun, Pupa U. P. A. Gilbert, Iryna Polishchuk, Boaz Pokroy, Julia Mahamid, Yael Politi, Steve Weiner, Peter Werner, Sebastian Bette, Robert Dinnebier, Ute Kolb, Emil Zolotoyabko, Peter Fratzl†

†Corresponding author. Email: fratzl@mpikg.mpg.de

Published 25 January 2019, *Science* **363**, 396 (2019)
DOI: 10.1126/science.aav0210

This PDF file includes:

Other Supplementary Material for this manuscript includes the following:
(available at www.sciencemag.org/content/363/6425/396/suppl/DC1)

Data S1 (.cif)

Materials and Methods

Sample preparation

Analytical grade calcium chloride dihydrate ($CaCl_2 \cdot 2H_2O$), sodium carbonate decahydrate ($Na_2CO_3 \cdot 10H_2O$) and magnesium chloride hexahydrate ($MgCl_2 \cdot 6H_2O$) were purchased from Sigma-Aldrich and used as received. 50 mL of a one molar Mg-Ca solution was prepared by dissolving 0.01 mol $MgCl_2 \cdot 6H_2O$ and 0.04 mol $CaCl_2 \cdot 2H_2O$ in ultra-pure water. The carbonate solution was prepared by dissolving 2 mmol $Na_2CO_3 \cdot 10H_2O$ in 48 mL ultra-pure water. A computer controlled titration system (905 Titrando, Metrohm Ltd.) was utilized for these experiments.

In a typical experiment, 2 mL of calcium solution was dosed at a rate of 10 mL/min into a 100 mL reaction vessel filled with 48 mL of carbonate solution. The total volume of the solution after dosing was 50 mL and the theoretical concentrations of cations (Mg^{2+} and Ca^{2+}) and anions ($CO_3^{2-}$and HCO_3^-) were equal to 40 mM. The precipitates were extracted by fast vacuum filtering of the reaction solution and then rinsed with ethanol. The collected powders after filtration were further dried and stored in a vacuum desiccator for subsequent characterization.

For the experiments on the effects of $Mg^{2+}/(Mg^{2+}+Ca^{2+})$ ratio on the formation and crystallization of ACC in solution, the initial $Mg^{2+}/(Mg^{2+}+Ca^{2+})$ ratio was varied from 10% to 40%, whereas the carbonate concentration was raised from 5 to 40 mM. The calculated concentration of $(Mg^{2+}+Ca^{2+})$ is equal to the carbonate concentration after mixing. The reaction was indexed, as N_1(MgACC)-N_2(mM), where N_1 corresponds to the initial $Mg^{2+}/(Mg^{2+}+Ca^{2+})$ ratio multiplied by 100, and N_2 corresponds to the carbonate concentration (as shown in legends in Fig. S4).

Monitoring pH and calcium concentration in solution

The pH and calcium concentration of the solution during reaction were monitored using a pH electrode and a calcium-sensitive electrode (Ca-ISE, Metrohm Ltd.) connected to the titration system. Electrodes, vessel, and burette tips were cleaned with dilute hydrochloric acid and carefully rinsed with distilled water after each experiment. The Ca-ISE was calibrated before every experiment by dosing the 1 M calcium solution to 50 ml water at room temperature at a rate of 0.1 mL/min, and measuring the signal (in mV), as a function of calcium concentration. During the calibration of calcium concentration, the pH of the solution was kept at 10.5 by titrating 0.01M NaOH. The pH-electrode was calibrated every day using standard buffers at pH 4.00, pH 7.00 and pH 9.00 (Metrohm Ltd.).

Scanning electron microscopy and transmission electron microscopy

The sample morphology was imaged using a field emission scanning electron microscope (JEOL, JSM-7500F) working at 5 kV. Samples were not coated prior investigation. Transmission electron microscopy was performed using a ZEISS, EM 912 transmission electron microscope operating at 120 kV.

X-ray powder diffraction

The laboratory X-ray diffraction (XRD) measurements were carried out in the Bragg-Brentano scattering geometry, using a Bruker D8-Advance X-ray powder diffractometer (Cu K_α radiation, $\lambda = 1.5406$ Å) in the 2θ-range of 10–80° and scan speed of 0.36 °/min. High-resolution X-ray powder diffraction (HRXRPD) measurements were performed at the dedicated beamline

ID22 of the European Synchrotron Radiation Facility (ESRF, Grenoble, France) using a wavelength of 0.49596 Å. Total X-ray scattering patterns were acquired continuously at ID11 beamline of ESRF using a beam-size of 1×1 mm^2 in cross-section. X-ray energy was set to 87 keV (wavelength, $\lambda = 0.142511$ Å). Data was acquired using a Frelon2K or Frelon4M detector with a 10–30 s integration time and processed with Fit2D software (*31*). Pair distribution functions (PDF) were produced using the PDFgetX3 software (*32*).

X-ray absorption near-edge structure (XANES) spectroscopy

The XANES spectra for oxygen K-edge and calcium L-edge were acquired by photoemission electron microscopy (PEEM) at the Advanced Light Source (ALS), Lawrence Berkeley National Laboratory (CA, USA) on beamline 11.0.1. The Ca spectrum in Fig. S2 is averaged over 237 single-pixel spectra and the O spectrum is averaged over 105 single-pixel spectra, acquired between 340-360 eV and 525-555 eV, respectively. The energy step between PEEM images was 0.1 eV in the central peak-containing region and 0.5 eV in the featureless pre- and post-edge energy regions. Both Ca and O spectra were extracted from two separate movies acquired on different areas and in repeated acquisitions. The O spectrum is normalized to a background intensity acquired on the pure platinum coating. Both O and Ca spectra are presented in comparison with those collected with other calcium carbonate minerals (*33*). All spectra were first aligned, so the O spectra had their peak (marked as 1 in Fig. S2) at 534 eV, and the Ca spectra had the L_2 main peak at 352.6 eV. These two alignment energy positions are indicated in Fig. S2 by two black vertical lines that run across the plots. All spectra, taken from CCHH ($CaCO_3 \cdot 0.5H_2O$) and other minerals, were peak-fitted again using the GG Macros (https://home.physics.wisc.edu/gilbert/software/), because several fine details of the spectra were discovered after the publication (*33*), e.g. the small pre-edge peaks at approximately 347 eV in calcite and vaterite, which also exist in CCHH. The energy positions obtained from accurate peak fitting are displayed as black vertical lines in O spectra (Fig. S2C) and as black vertical segments in Ca spectra (Fig. S2D).

The XANES spectra at the Ca K-edge were acquired at the LUCIA beamline at the SOLEIL Synchrotron Light Source (Saint-Aubin, France). The X-ray beam energy was varied from 4000 to 4080 eV in 1.0 eV steps before the pre-edge and in 0.2 eV steps thereafter. The electron energy in the synchrotron storage ring was 2.75 GeV and the current was up to 400 mA. The X-ray energy was selected by a double-crystal Si(111) monochromator, which was calibrated using Ti foil and setting the edge at 4966 eV. The beam size of the sample was ca. 1.5×1.5 mm^2. Powder samples of CCHH, ACC, vaterite, aragonite and calcite were mounted with a sticky tape. To improve the signal-to-noise ratio, all spectra were averaged over three to five scans. Baseline subtraction and normalization were performed using the ATHENA of the IFEFFIT software package (*34*). The edge energy was determined at the maximum of the third peak of the first derivative of the XANES data. Normalization was performed using a linear pre-edge function and a quadratic polynomial for the post-edge.

Automated electron diffraction tomography (ADT)

Three-dimensional electron diffraction data acquisitions were performed in the Johannes Gutenberg-Universität, Mainz with a FISCHIONE tomography sample holder cooled with liquid N_2, using the ADT acquisition module (*35*) developed for FEI TECNAI F30 TEM. A condenser aperture of 10 µm and mild illumination setting (gun lens 8 and spot size 6) were used in order to

produce a quasi-parallel beam of 50 nm in diameter on the sample and reduce the electron irradiation dose. Sample image tracking was performed in the microprobe HAADF-STEM mode, whereas electron diffraction was acquired with nano-electron diffraction (NED) setting. ADT tilt series were collected both with and without precession of the beam. Precession electron diffraction (PED) was used in order to improve the reflection intensity integration quality (*36*) and only ADT/PED data were used for structure solution. PED was performed using the SpinningStar unit developed by NanoMEGAS Company, Belgium. The precession angle was kept at 1.2°. For data processing and extraction, a ADT software (developed in the group of Dr. Kolb, Johannes Gutenberg-University Mainz, Germany and distributed by the NanoMegas Company, Belgium) was used, including three-dimensional diffraction reconstruction and visualization, cell determination based on clustering routines (*37*), and reflection intensity integration (*36, 38, 22*).

Structure solution based on ADT data

STEM imaging revealed crystals with two different morphologies, as presented in Fig. S8. Type-1 crystals (left panel) are thin and elongated needles which produce single crystal diffraction only at the tip. Crystals of the second type (middle panel) are thin needle-like platelets. Four ADT data sets were taken from crystals exhibiting type-1 morphology, which can be accounted to the majority of the detected crystals. The cell parameters, as shown in Table S4, and used for data extraction, were found in all these data sets to be similar within the expected error bars. Extinctions follow the rule (*h0l*) with *l* = 2n, indicating the *c*-glide plane perpendicular to the *b*-axis (see Fig. S8, right panel). Due to preferred orientation for all data sets the b-axis was situated inside the missing cone.

Two data sets (indicated as Cr-1 and Cr-2 in Table S5) provided a reasonable coverage of the reciprocal space (>50%) for structure solution in space group $P2_1/c$. *Ab initio* structure solution was performed in kinematic approximation ($I \sim F^2(hkl)$) by direct methods, as implemented in the program SIR2014 (*39*). Scattering factors for electrons were taken from Doyle and Turner (*40*). The remaining two data sets were successfully used for structure solution with comparable results applying a resolution limit of 1 Å. In order to increase the coverage of the reciprocal space data set Cr-2 (tilt approximately around (1-11)) and Cr-3 (tilt approximately around (-101)) were merged (R_{int}=0.169), see Table S5. The *ab initio* structure solution using SIR2014 converged to a final residual R(F) of 0.219. The potential map shows two strongest maxima (3.01, 3.51 eÅ^3) corresponding to two Ca atoms. The next nine maxima resemble the carbonate groups (1.18 to 0.75 eÅ^3) and one maximum at 0.48 eÅ^3 indicates the water oxygen. The residual potential has a height of 0.39 eÅ^3 and is situated in the vicinity (approx. 1.5 Å) of Ca and O_{CO3}. Isotropic temperature factors, Uiso, were found independently for each atom of the carbonate group to be between 0.03 to 0.09 Å^2.

Subsequent SHELXL (*41*) refinement converged to a residual R(F) of 28% for a two sigma threshold, which is common for beam sensitive material solved by electron diffraction tomography (42). The coverage of independent reflections of 62% leads to an elongation of scattering potentials in direct space causing some errors in temperature factor and C-O distances. Thus, an overall Uiso for carbonate atoms and the SADI extraction was used leading to C-O distances of 1.22, 1.24, 1.41 and 1.29, 1.35, 1.38 Å. Nevertheless, as is seen in Fig. S9, the carbonate groups are nearly planar. Both types of Ca positions are eightfold coordinated (Fig. S9, right panel).

Additionally, ADT diffraction data were collected from crystals showing morphology of type 2. From the reconstructed volumes, the cell parameters were extracted and given in Table S4. Only reflections with $k = 2n$ along the b^*-axis of reciprocal space could be detected. A structure solution has not been undertaken since the coverage of the reciprocal space was too low.

Raman and infrared (IR) spectroscopy

Raman spectra were collected using a confocal Raman microscope (α300; WITec) equipped with a Nikon objective (10×) and a 532 nm laser. Spectra were acquired with a CCD camera (DV401-BV; Andor) behind a spectrometer (UHTS 300; WITec) (40 accumulations, integration time 1 s). The ACC powders were dropped on a microscope slide just before individual measurement. IR spectra were recorded on a pellet with KBr and the sample using a Fourier transform infrared spectrometer (Bruker Optik GmbH) equipped with a MCT-detector (32 scans, resolution 4 cm^{-1}).

Thermogravimetric analysis/differential scanning calorimetry

Weight loss and heat flow were simultaneously measured during programmed heating (25-500 °C, at the rate of 1.5 °C/min) using thermogravimetric analysis coupled with differential scanning calorimetry (SENSYS evo TGA-DSC, SETARAM Instrumentation, Caluire, France). For these measurements, nearly 15 mg of the dried powders were placed in an alumina crucible. Dry nitrogen was used as the purge gas.

ICP-OES analysis

Element analysis was performed by inductively coupled plasma-optical emission spectrometry (PerkinElmer, Optima 8000 ICP-OES Spectrometer). Sample solutions were prepared by dissolving certain amounts of as-prepared powders in the diluted HNO_3 solution.

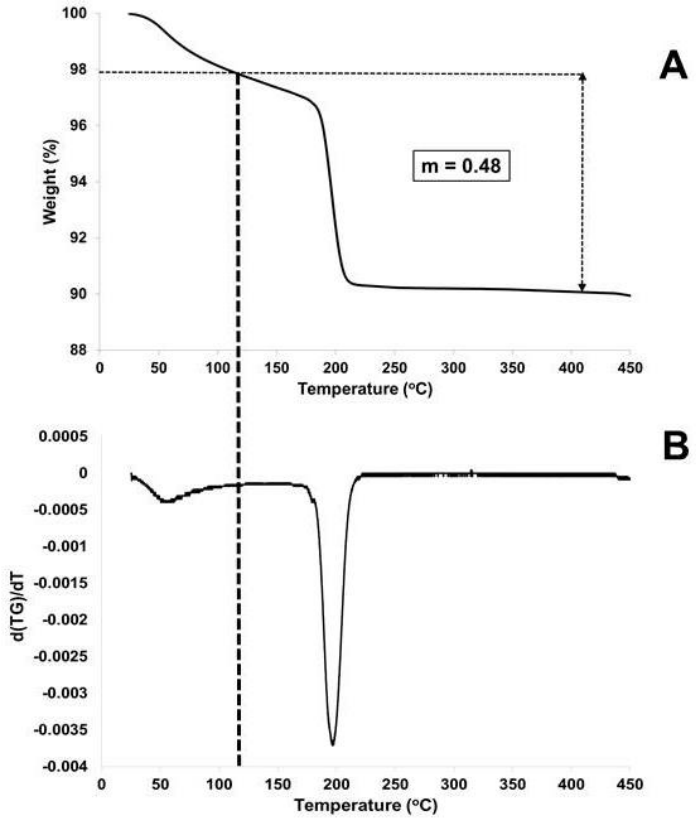

Fig. S1.

The results of TGA in CCHH. Temperature-dependent weight loss (A) and its derivative (B) measured upon heating at a rate of 1.5 °C/min. Weight loss below 115 °C (vertical dashed line) occurs due to evaporation of the absorbed water (first dip in (B)), while above this temperature and up to nearly 450 °C, the discharge of structural water is observed with the maximum release rate at about 200 °C (second dip in (B)). Counting the weight loss of structural water between 115 and 400 - 450 °C (dotted arrow in (A)) yields chemical formula of CCHH, $CaCO_3 \cdot mH_2O$, with m = 0.48.

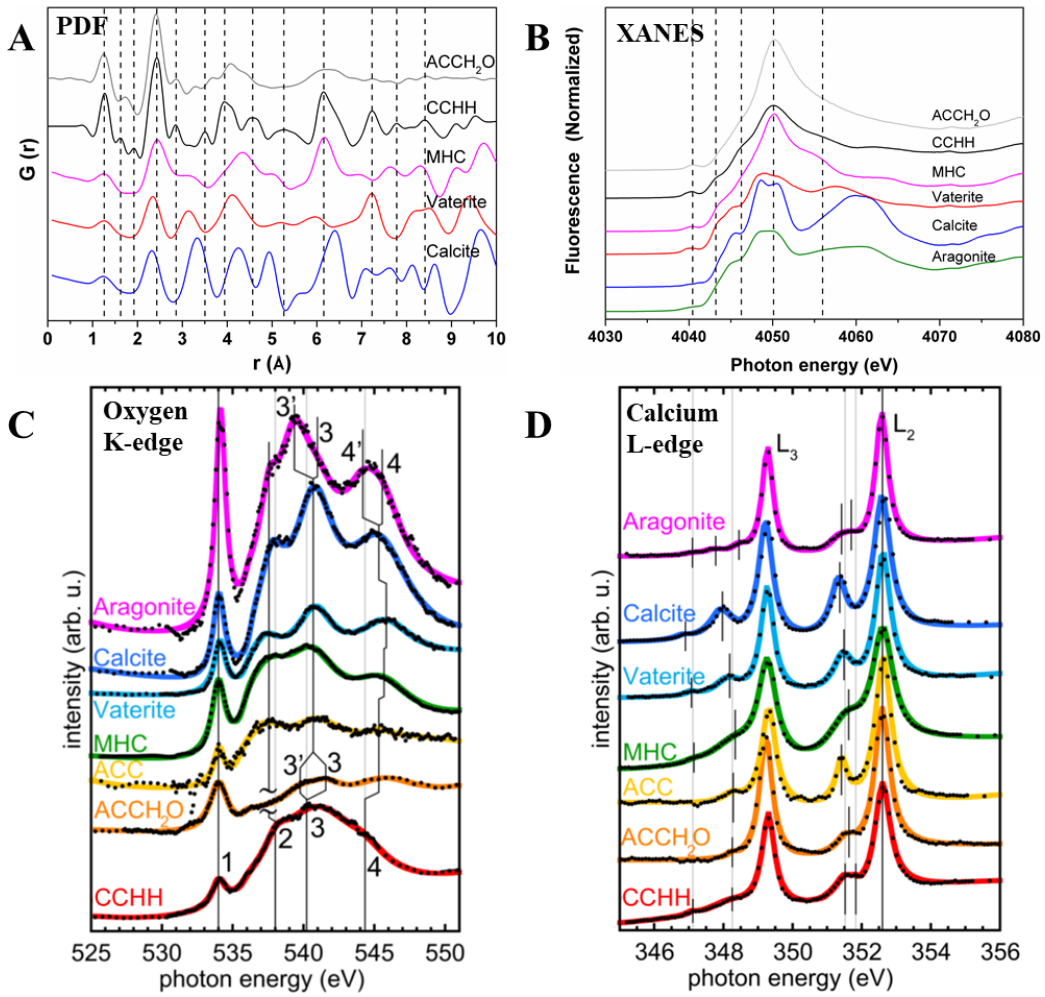

Fig. S2.

PDF patterns (A), Ca K-edge XANES spectra (B), oxygen K-edge XANES spectra (C) and Ca L-edge XANES spectra (D) of CCHH and other known calcium carbonate phases. The PDF pattern of CCHH shows some similarities to hydrated ACC ($ACC \cdot 1H_2O$) and MHC, but differs from those of vaterite and calcite. For example, the most intense PDF peak of CCHH occurs at ~2.44 Å (attributed to the average Ca-O bond distance), which is similar to that of ACC and MHC, but its relative intensity is much higher than that in MHC. Moreover, while ACC shows only short range order up to 6 - 7 Å, the order in CCHH extends above 10 Å, similarly to other crystalline phases. The Ca K-edge XANES spectrum of CCHH also differs from those known for other calcium carbonate phases. The pre-edge feature at ~4040.4 eV (attributed to 1s→3d transition, indicative of a non-centrosymmetric coordination) is similar to both ACC and MHC, but the general shape of the spectrum is more similar to that of MHC. The multiple-scattering peak at 4046 eV is indicative of increased order relative to ACC and the edge shape including intra-atomic transitions (shoulders at 4044 – 4046 eV) are similar to those observed in MHC. In (C) and (D), the experimental data are represented by black dots, whereas the peak-fitted spectra - by colored solid lines. Black vertical lines indicate the position of each peak found by peak fitting, the light gray vertical lines indicate the peak positions for CCHH, thus making it easier to see the difference between CCHH and all other calcium carbonate phases. The oxygen

K-edge spectrum of CCHH differs from those known for all other calcium carbonate crystalline or amorphous mineral phases. In particular, the peak, marked as 4, appears at 544 eV in CCHH and at 545 - 546 eV in all other phases. The calcium L-edge spectrum of CCHH resembles in shape that of ACC·1H_2O, but shows an additional small peak in the pre-L_3-edge at 347.1 eV, which appears at similar energies only in crystalline calcite, vaterite, MHC, and aragonite. Moreover, only CCHH and aragonite have two peaks in the pre-L_2-edge region, but in CCHH these are at 351.5 and 351.8 eV, while in aragonite they appear at lower energies. The collected XANES spectra, therefore, demonstrate that CCHH is distinct from all other calcium carbonate phases.

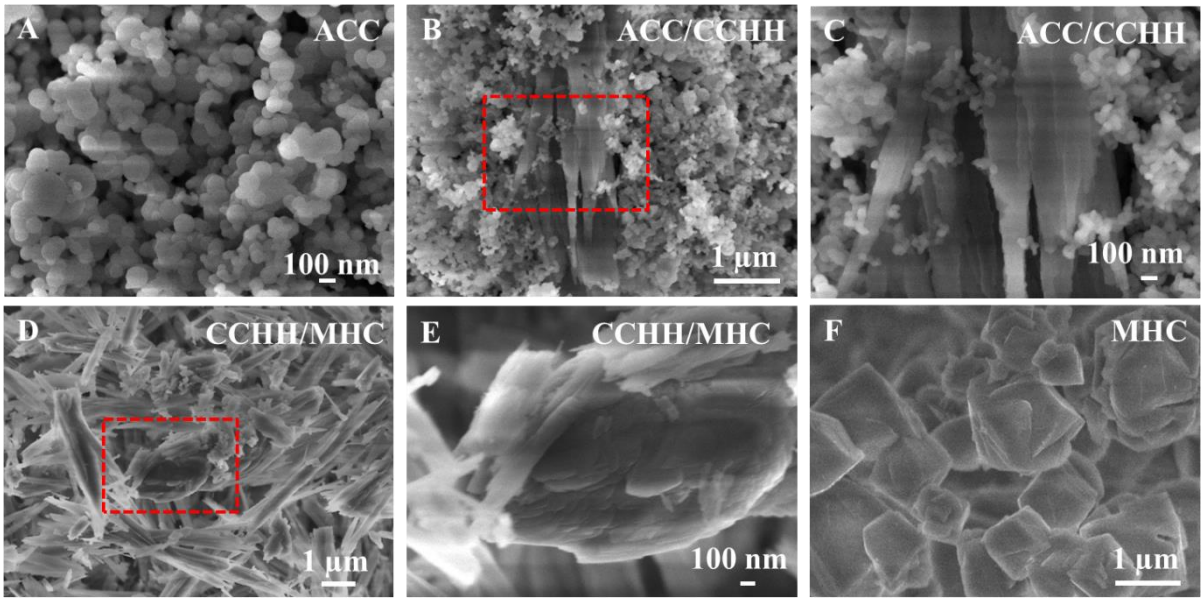

Fig. S3.

SEM images of ACC nanoparticles (A), coexistence of ACC nanoparticles and CCHH crystals (B, C), coexistence of CCHH and MHC crystals (D, E) and MHC crystals (F). The initially precipitated Mg-containing ACC nanoparticles have spherical shapes with an average diameter of 71 ± 28 nm, which is similar to the pure ACC, synthesized at a calcium carbonate concentration of 40 mM. During growth of CCHH crystals, some of these nanoparticles are attached to the needle-like crystals (within red rectangle in (B) and in image (C)), suggesting a possibility of local dissolution/re-precipitation. During the CCHH/MHC transformation, the CCHH needles are attaching to the surface of MHC crystals (within red rectangle in (D) and in image (E)), resulting in the micrometer-sized MHC crystals with well-developed facets, visible in image (F).

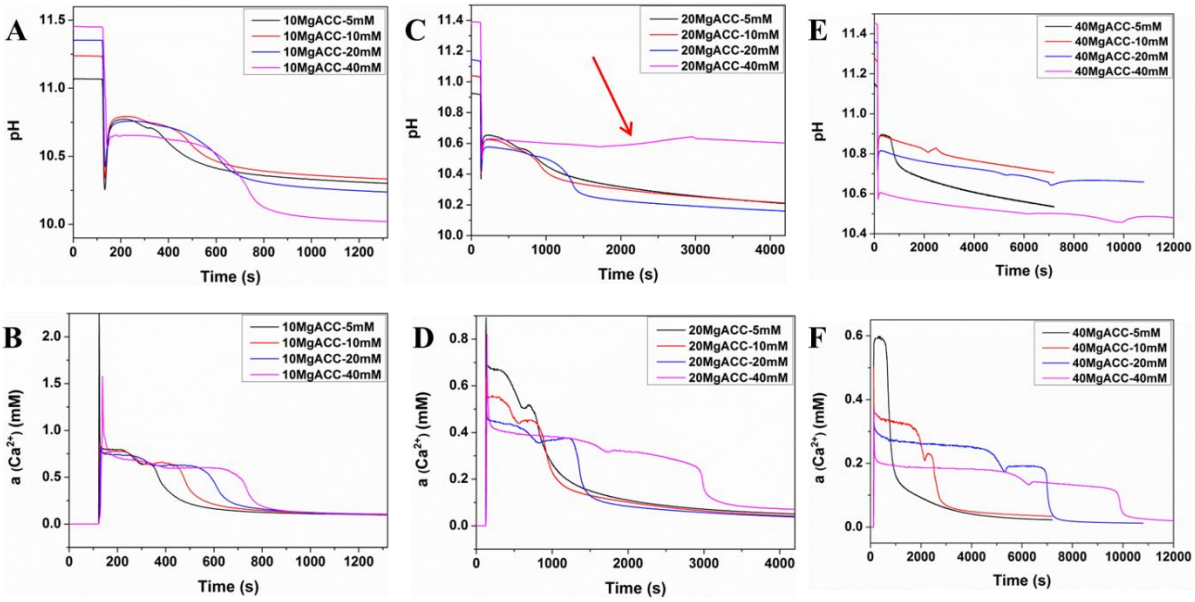

Fig. S4.

The pH (A, C, E) and Ca^{2+} activity (B, D, F) change in the solution for all investigated reactions. For 10% Mg^{2+} reactions (A, B), similar to the pure system, both pH and Ca^{2+} activity decrease rapidly within 10 min, indicating fast crystallization of crystalline calcium carbonate polymorphs with lower solubility. For 20% Mg^{2+} in the range of 5 – 20 mM (C, D) and 40% Mg^{2+} at 5 mM (E, F), the curves are similar to the 10% Mg^{2+} reactions. However, for 20% Mg^{2+} at 40 mM (C, D) and 40% Mg^{2+} at 10 mM (E, F), the pH shows an abnormal increase for about 20 min (marked by red arrow in C), followed by the gradual decrease. For 40% Mg^{2+} at 20 and 40 mM, the pH curves reveal two sudden drops in pH after which the pH stabilizes, in accordance with the step-wise decrease in Ca^{2+} activity. Line colors are indicated in the respective inserts.

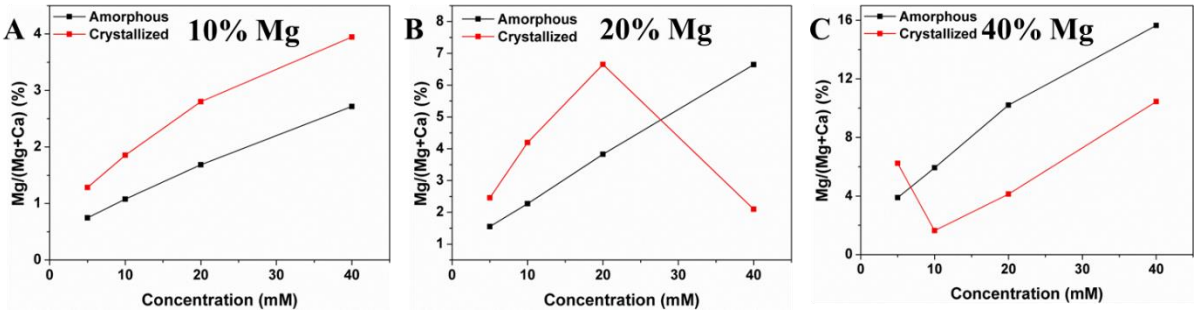

Fig. S5.

$Mg^{2+}/(Mg^{2+}+Ca^{2+})$ ratio in the amorphous and crystallized samples prepared with different amounts of Mg^{2+} and overall carbonate concentrations (A-C). As the particle size of ACC decreases with increasing concentrations, the Mg^{2+} content in ACC increases slightly with decreasing particle size. After crystallization, lower Mg^{2+} incorporation in ACC (< 5%) resulted in the increased Mg^{2+} content in the crystallized products (i.e. calcite), while higher Mg^{2+} incorporation in ACC (> 5%) resulted in the significantly lower Mg^{2+} content in the crystallized products (i.e. MHC or CCHH).

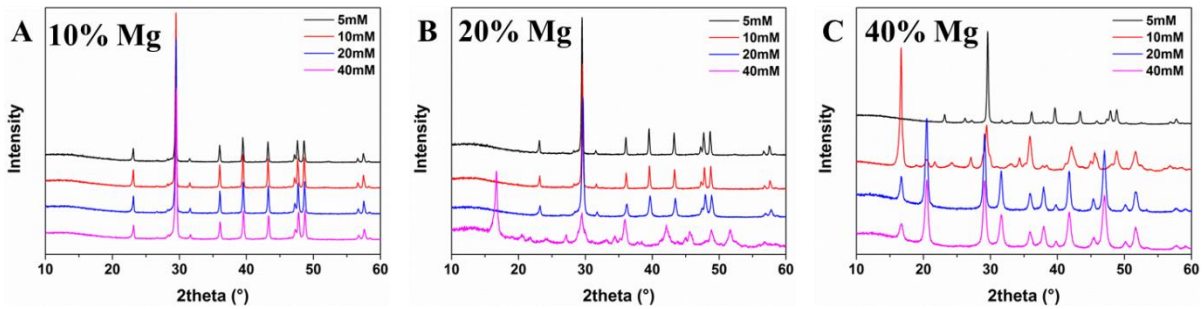

Fig. S6.

Laboratory XRD patterns taken after sample crystallization. For 10% Mg^{2+} at all concentrations (A), as well as for 20% Mg^{2+} at 5 – 20 mM (B) and 40% Mg^{2+} at 5 mM (C), all crystallized samples show Mg^{2+}-calcite. For 20% Mg^{2+} at 40 mM (B) and 40% Mg^{2+} at 10 mM (C), CCHH is obtained. For 40% at 20 and 40 mM (C), pure MHC is formed. Line colors are indicated in the respective inserts.

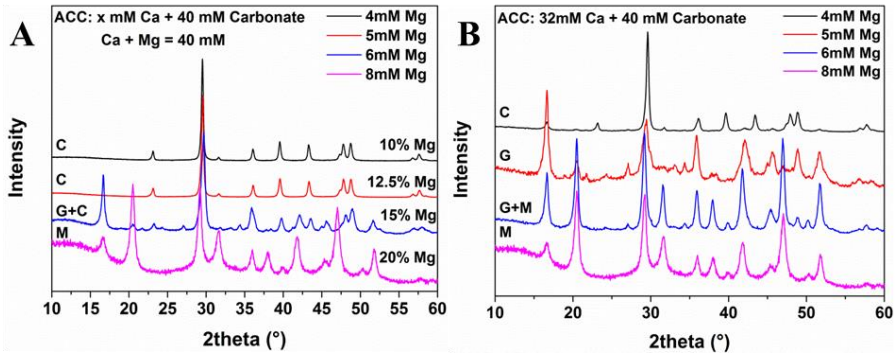

Fig. S7.

Laboratory XRD patterns of crystallized samples prepared by adding first a 1M $CaCl_2$ solution to 40 mM Na_2CO_3 solution and then adding a 1M $MgCl_2$ solution. In (A), variable amounts of Ca^{2+} and Mg^{2+} are used, while keeping the total concentration of Ca^{2+} and Mg^{2+} equal to the concentration of carbonate. In (B), fixed amount of Ca^{2+} (32 mM) was added to 40 mM carbonate solution to produce ACC and then variable amounts of Mg^{2+} were added to the solution with the final concentrations of Mg^{2+} to be 4, 5, 6, and 8 mM. These data demonstrate that the solution concentration of Mg^{2+} indeed determines the polymorph selection, since CCHH can also be obtained when Mg^{2+} is not incorporated in ACC at all. Line colors are indicated in the respective inserts.

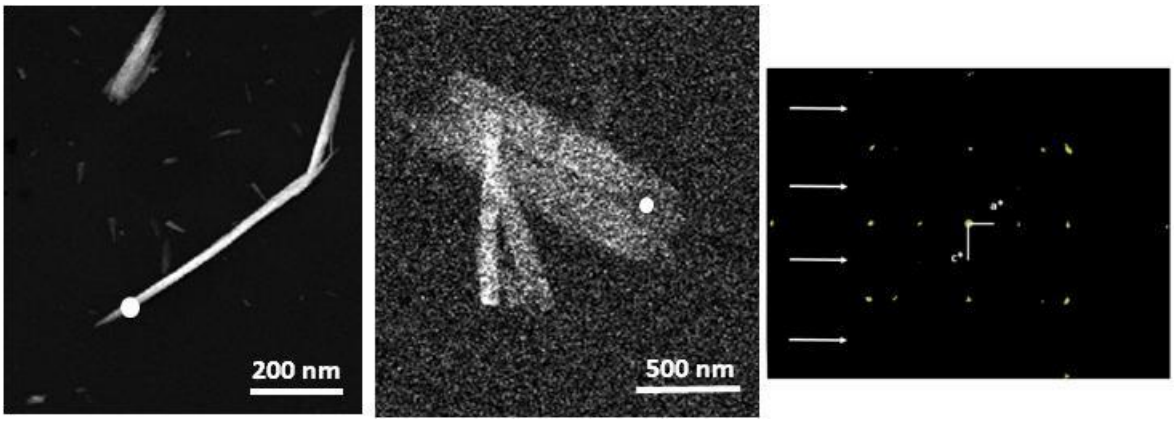

Fig. S8.

STEM images of the detected crystal morphologies. Thin needles of CCHH ($CaCO_3 \cdot ½H_2O$) crystals (left panel) and thin needle-like platelets (middle panel). Electron beam sizes and positions used for ADT data acquisition are indicated as white spots in the left and middle panels. In right panel, a slice of the [010] zone cut from 3D reconstruction of ADT data set is shown. Extinctions due to the *c*-glide plane are indicated as white arrows (right panel).

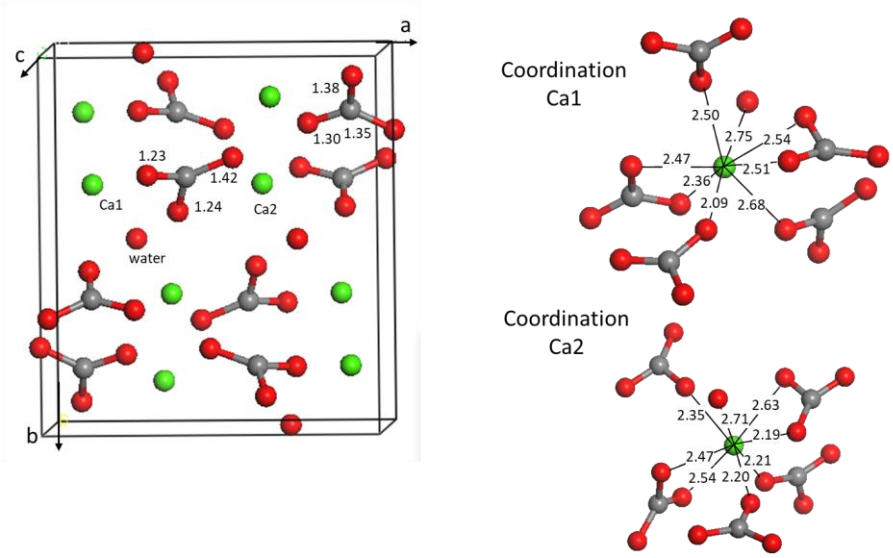

Fig. S9.

Crystal structure of CCHH ($CaCO_3 \cdot ½H_2O$), including C-O distances (left panel) and coordination spheres for both types of Ca atomic positions (right panel).

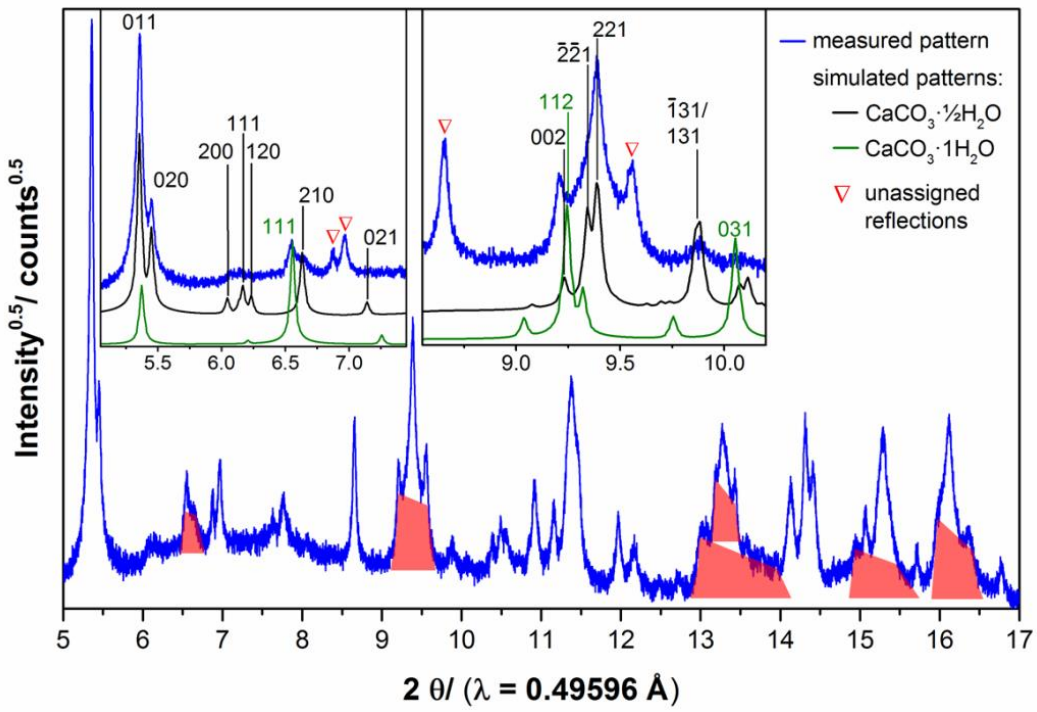

Fig. S10.

Synchrotron HRXRPD pattern of CCHH ($CaCO_3 \cdot ½H_2O$) with several peaks of characteristic triangular shape (highlighted in red). These peaks indicate stacking fault-type lattice disorder in CCHH. Selected sections of the measured diffraction profile (see inserts) are compared to simulated patterns of CCHH and $CaCO_3 \cdot 1H_2O$ (MHC). While the (011), (020) and (221) reflections originated from CCHH are rather sharp, the (200), (111), (120), (210), (021), ($\bar{1}$31) and (131) reflections are vastly broadened; they almost merge with the background. In addition, there are extra reflections (marked by red triangles in inserts) that cannot be assigned to CCHH or MHC. These reflections are originated from $CaCO_3 \cdot ¾H_2O$.

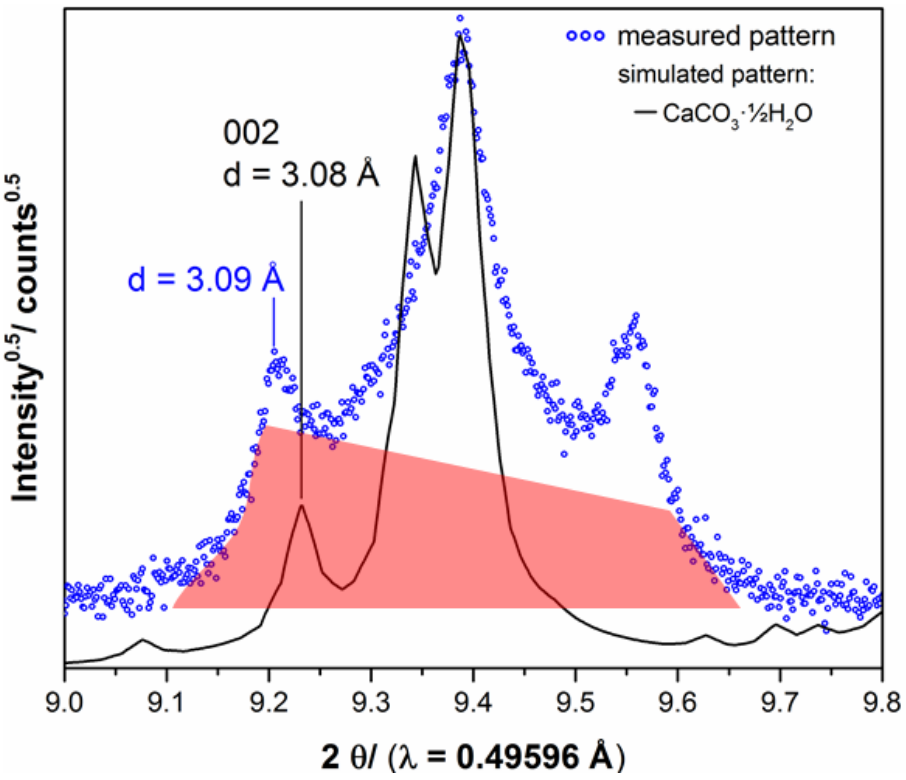

Fig. S11.

Excerpt of the measured synchrotron HRXRPD pattern of CCHH ($CaCO_3 \cdot ½H_2O$), magnifying the characteristic triangular peak shape of the (002)-reflection (highlighted by a red area).

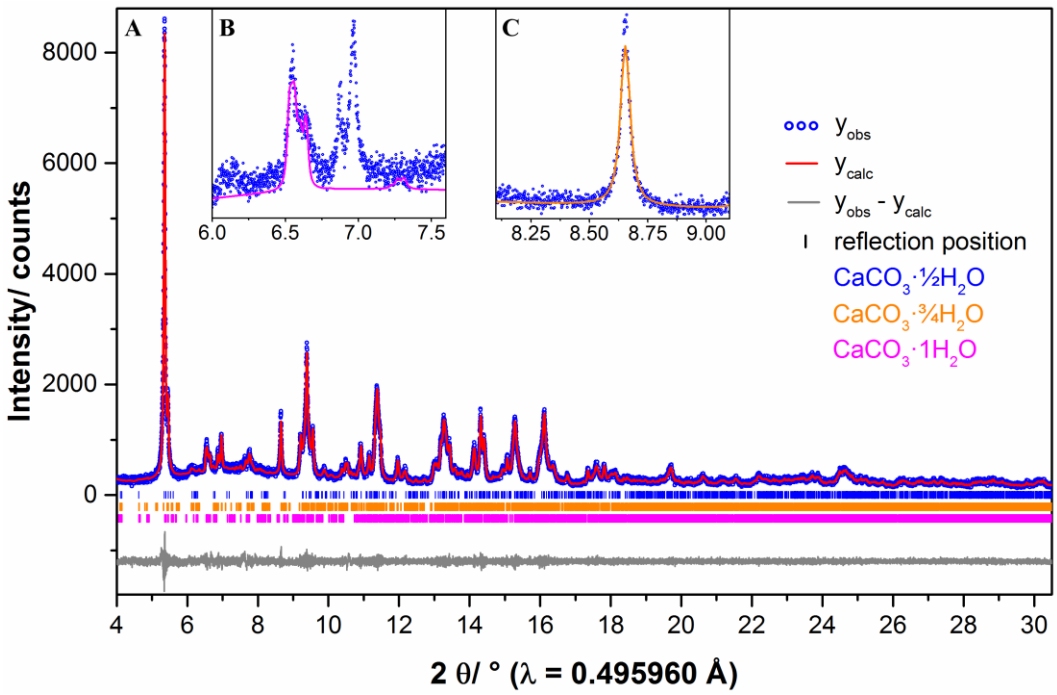

Fig. S12.

(A) Graphical results of the final fit to the measured synchrotron diffraction pattern (Rwp = 7.55 %) using the unit cells of CCHH ($CaCO_3 \cdot ½H_2O$), $CaCO_3 \cdot ¾H_2O$, and MHC ($CaCO_3 \cdot 1H_2O$). Constraints on the lattice parameters were applied to simulate commensurate faulting in the *c*-direction referring to CCHH. Inserts (B) and (C) show magnified fits near specific diffraction peaks located, respectively, at 2θ = 6.5° (d = 4.37 Å) and 2θ = 8.7° (d = 3.27 Å).

Table S1.

Chemical composition of CCHH. The Ca^{2+}, Mg^{2+} and Na^{+} contents were measured using ICP, whereas the full water amount - by TGA, as weight loss between room temperature and 300 °C. Each measurement was repeated five times to obtain the most reliable data.

Composition	Ca^{2+} (wt%)	Mg^{2+} (wt%)	Na^{+} (wt%)	H_2O (wt%)	CO_3^{2-} (wt%)
	34.92 ± 0.24	0.41 ± 0.08	0.06 ± 0.03	10.05 ± 0.53	54.50 ± 0.23

Table S2.

Peak positions in the Raman and IR spectra of CCHH and peak assignment to different vibration modes.

Raman (cm^{-1})	Infrared (cm^{-1})	Assignment
3382 3285	3379 3290	Anti- and symmetric OH stretch $\nu_{OH}(B_2)$
1661	1659	HOH bending $\nu_{HOH}(A_1)$
1579 1483 1423	1524 1490 1392 1423	Asymmetric CO stretching $\nu_{CO}^{as}(E', \nu_3)$
1102	1096	Symmetric CO stretching $\nu_{CO}^{s}(A1', \nu_1)$
862	866 860	Out-of-plane bending $\pi_{CO}^{as}(A2'', \nu_2)$
731 700	723 692	In-plane bending $\delta_{CO}^{as}(E', \nu_4)$
212 266 297		Lattice vibrations

Table S3.

The $Mg^{2+}/(Mg^{2+}+Ca^{2+})$ in ACC and the Mg^{2+}/Ca^{2+} in solution at different reaction conditions. Mg^{2+} ions were added into the reaction solution immediately after the precipitation of ACC.

Carbonate (mM)	Mg^{2+} (mM)	$Mg^{2+}+Ca^{2+}$ (mM)	Initial $Mg^{2+}/(Mg^{2+}+Ca^{2+})$	$Mg^{2+}/(Mg^{2+}+Ca^{2+})$ in ACC	Mg^{2+}/Ca^{2+} in solution	Crystalline phase
40mM	4	36	0.111	0.007614	3.5460	Calcite
40mM	5	37	0.135	0.00897	4.6764	CCHH
40mM	6	38	0.158	0.010035	4.9313	MHC
40mM	8	40	0.2	0.013706	5.8047	MHC
40mM	4	40	0.125	0.006361	2.6865	Calcite
40mM	5	40	0.15	0.008348	3.9544	CCHH
40mM	6	40	0.15	0.047261	2.4268	Calcite

Table S4.

Lattice parameters of the original unit cells of CCHH ($CaCO_3 \cdot ½H_2O$), $CaCO_3 \cdot ¾H_2O$, and MHC ($CaCO_3 \cdot 1H_2O$), as well as the transformed unit cells (metric of CCHH).

	original unit cells		
	$CaCO_3 \cdot ½\ H_2O$	**$CaCO_3 \cdot ¾\ H_2O$**	**$CaCO_3 \cdot 1\ H_2O$ (*43*)**
space group	$P2_1/c$	$P2_1$	$P3_1$
Z	8	8	9
***V*/ Å³**	600.17	610.55	727.73
***a*/ Å**	9.33	9.51	10.55
***b*/ Å**	10.44	6.16	10.55
***c*/ Å**	6.16	11.26	7.55
***α*/ °**	90	90	90
***β*/ °**	90.5	112.3	90
***γ*/ °**	90	90	120

	transformed unit cells for commensurate defects						
	$CaCO_3 \cdot ½\ H_2O$	**$CaCO_3 \cdot ¾\ H_2O$**			**$CaCO_3 \cdot 1\ H_2O$ (*43*)**		
		trans-formation		**mismatch**	**trans-formation**		**mismatch**
Z	8		16	-		18	-
***V*/ Å³**	600.17	$V' = 2 \cdot V$	1221.20	-	$V' = 2 \cdot V$	1455.46	-
***a*/ Å**	9.33	$a' = a$	9.51	1.93 %	$a' = 2 \cdot b^*$	18.28	2.04 %
***b*/ Å**	10.44	$b' = 2 \cdot c^*$	20.86	0.01 %	$b' = a$	10.55	1.05 %
***c*/ Å**	6.16	$c' = b$	6.16	0.00 %	$c' = c$	7.55	22.56 %
***α*/ °**	90	$\alpha' = \alpha$	90	-	$\alpha' = \beta$	90	-
***β*/ °**	90.5	$\beta' = \gamma$	90	-	$\beta' = \alpha$	90	-
***γ*/ °**	90	$\gamma' = \beta^*$	90	-	$\gamma' = \gamma^*$	90	-

Table S5.

Quality parameters of ADT data sets for four measured CCHH crystals.

Crystal	R_{int} /%	Coverage of independent reflections, %	Overall B_{iso} , $Å^2$	Independent reflections	R(F)
Cr-1	17.7	55	2.55	314	0.271
Cr-2	17.1	59	2.63	376	0.293
Cr-3	13.9	37	1.25	232	-
Cr-4	15.3	40	2.08	252	-
Cr-2/Cr-3	16.9	62	2.35	392	0.219

Table S6.

Refined lattice parameters of the unit cells of CCHH ($CaCO_3 \cdot ½H_2O$), $CaCO_3 \cdot ¾H_2O$, and MHC ($CaCO_3 \cdot 1H_2O$) used to simulate commensurate faulting in the *c*-direction, referring to the structure of CCHH.

	$CaCO_3 \cdot ½\ H_2O$	**$CaCO_3 \cdot ¾\ H_2O$**	**$CaCO_3 \cdot 1\ H_2O$**
space group	*P*1	*P*1	*P*1
Z	8	16	18
***V*/ Å³**	588.46(4)	1175.50(4)	1448.78(4)
***a*/ Å**	9.1922(1)	9.1922(1)	18.3843(2)
***b*/ Å**	10.4180(2)	20.8360(4)	10.4180(2)
***c*/ Å**	6.1461(4)	6.1393(1)	7.5647(1)
***α*/ °**	90.57(1)	87.70(1)	89.64(1)
***β*/ °**	90.87(1)	89.67(1)	89.88(1)
***γ*/ °**	89.56(1)	89.56(1)	89.56(1)

Data S1.
The CIF-file (CCHH.cif) for calcium carbonate hemihydrate

References and Notes

1. J. W. Beck, R. L. Edwards, E. Ito, F. W. Taylor, J. Recy, F. Rougerie, P. Joannot, C. Henin, Sea-surface temperature from coral skeletal strontium/calcium ratios. *Science* **257**, 644–647 (1992). doi:10.1126/science.257.5070.644 Medline

2. F. J. Millero, The marine inorganic carbon cycle. *Chem. Rev.* **107**, 308–341 (2007). doi:10.1021/cr0503557 Medline

3. M. Cusack, A. Freer, Biomineralization: Elemental and organic influence in carbonate systems. *Chem. Rev.* **108**, 4433–4454 (2008). doi:10.1021/cr078270o Medline

4. S. Goffredo, F. Prada, E. Caroselli, B. Capaccioni, F. Zaccanti, L. Pasquini, P. Fantazzini, S. Fermani, M. Reggi, O. Levy, K. E. Fabricius, Z. Dubinsky, G. Falini, Biomineralization control related to population density under ocean acidification. *Nat. Clim. Chang.* **4**, 593–597 (2014). doi:10.1038/nclimate2241 Medline

5. L. B. Gower, Biomimetic model systems for investigating the amorphous precursor pathway and its role in biomineralization. *Chem. Rev.* **108**, 4551–4627 (2008). doi:10.1021/cr800443h Medline

6. L. J. de Nooijer, H. J. Spero, J. Erez, J. Bijma, G. J. Reichart, Biomineralization in perforate foraminifera. *Earth Sci. Rev.* **135**, 48–58 (2014). doi:10.1016/j.earscirev.2014.03.013

7. D. Gebauer, A. Völkel, H. Cölfen, Stable prenucleation calcium carbonate clusters. *Science* **322**, 1819–1822 (2008). doi:10.1126/science.1164271 Medline

8. M. H. Nielsen, S. Aloni, J. J. De Yoreo, In situ TEM imaging of $CaCO_3$ nucleation reveals coexistence of direct and indirect pathways. *Science* **345**, 1158–1162 (2014). doi:10.1126/science.1254051 Medline

9. J. W. Morse, R. S. Arvidson, A. Lüttge, Calcium carbonate formation and dissolution. *Chem. Rev.* **107**, 342–381 (2007). doi:10.1021/cr050358j Medline

10. Y. Politi, T. Arad, E. Klein, S. Weiner, L. Addadi, Sea urchin spine calcite forms via a transient amorphous calcium carbonate phase. *Science* **306**, 1161–1164 (2004). doi:10.1126/science.1102289 Medline

11. L. Addadi, S. Raz, S. Weiner, Taking advantage of disorder: Amorphous calcium carbonate and its roles in biomineralization. *Adv. Mater.* **15**, 959–970 (2003). doi:10.1002/adma.200300381

12. L. Addadi, D. Joester, F. Nudelman, S. Weiner, Mollusk shell formation: A source of new concepts for understanding biomineralization processes. *Chemistry* **12**, 980–987 (2006). doi:10.1002/chem.200500980 Medline

13. Y. U. T. Gong, C. E. Killian, I. C. Olson, N. P. Appathurai, A. L. Amasino, M. C. Martin, L. J. Holt, F. H. Wilt, P. U. P. A. Gilbert, Phase transitions in biogenic amorphous calcium carbonate. *Proc. Natl. Acad. Sci. U.S.A.* **109**, 6088–6093 (2012). doi:10.1073/pnas.1118085109 Medline

14. W. Sun, S. Jayaraman, W. Chen, K. A. Persson, G. Ceder, Nucleation of metastable aragonite CaCO3 in seawater. *Proc. Natl. Acad. Sci. U.S.A.* **112**, 3199–3204 (2015). doi:10.1073/pnas.1423898112 Medline

15. Z. Zou, L. Bertinetti, Y. Politi, A. C. S. Jensen, S. Weiner, L. Addadi, P. Fratzl, W. J. E. M. Habraken, Opposite particle size effect on amorphous calcium carbonate

crystallization in water and during heating in air. *Chem. Mater.* **27**, 4237–4246 (2015). doi:10.1021/acs.chemmater.5b00145

16. F. A. Andersen, L. Brecevic, G. Beuter, D. B. Dell'Amico, F. Calderazzo, N. J. Bjerrum, A. E. Underhill, Infrared spectra of amorphous and crystalline calcium carbonate. *Acta Chem. Scand.* **45**, 1018–1024 (1991). doi:10.3891/acta.chem.scand.45-1018

17. W. D. Bischoff, S. K. Sharma, F. T. Mackenzie, Carbonate ion disorder in synthetic and biogenic magnesium calcites: A Raman spectral study. *Am. Mineral.* **70**, 581–589 (1985).

18. G. Behrens, L. T. Kuhn, R. Ubic, A. H. Heuer, Raman spectra of vateritic calcium carbonate. *Spectrosc. Lett.* **28**, 983–995 (1995). doi:10.1080/00387019508009934

19. H. H. Adler, P. F. Kerr, Infrared spectra, symmetry and structure relations of some carbonate minerals. *Am. Mineral.* **48**, 839–853 (1963).

20. R. L. Frost, M. J. Dickfos, Raman and infrared spectroscopic study of the anhydrous carbonate minerals shortite and barytocalcite. *Spectrochim. Acta A* **71**, 143–146 (2008). doi:10.1016/j.saa.2007.11.021 Medline

21. A. E. S. Van Driessche, L. G. Benning, J. D. Rodriguez-Blanco, M. Ossorio, P. Bots, J. M. García-Ruiz, The role and implications of bassanite as a stable precursor phase to gypsum precipitation. *Science* **336**, 69–72 (2012). doi:10.1126/science.1215648 Medline

22. U. Kolb, E. Mugnaioli, T. E. Gorelik, Automated electron diffraction tomography - a new tool for nano crystal structure analysis. *Cryst. Res. Technol.* **46**, 542–554 (2011). doi:10.1002/crat.201100036

23. B. E. Warren, X-ray diffraction in random layer lattices. *Phys. Rev.* **59**, 693–698 (1941). doi:10.1103/PhysRev.59.693

24. S. Bette, T. Takayama, K. Kitagawa, R. Takano, H. Takagi, R. E. Dinnebier, Solution of the heavily stacking faulted crystal structure of the honeycomb iridate $H_3LiIr_2O_6$. *Dalton Trans.* **46**, 15216–15227 (2017). doi:10.1039/C7DT02978K Medline

25. L. Kabalah-Amitai, B. Mayzel, Y. Kauffmann, A. N. Fitch, L. Bloch, P. U. P. A. Gilbert, B. Pokroy, Vaterite crystals contain two interspersed crystal structures. *Science* **340**, 454–457 (2013). doi:10.1126/science.1232139 Medline

26. E. Mugnaioli, I. Andrusenko, T. Schüler, N. Loges, R. E. Dinnebier, M. Panthöfer, W. Tremel, U. Kolb, Ab Initio structure determination of vaterite by automated electron diffraction. *Angew. Chem. Int. Ed.* **51**, 7041–7045 (2012). doi:10.1002/anie.201200845 Medline

27. G. Pawley, Unit-cell refinement from powder diffraction scans. *J. Appl. Cryst.* **14**, 357–361 (1981). doi:10.1107/S0021889881009618

28. M. M. J. Treacy, J. M. Newsam, M. W. Deem, A general recursion method for calculating diffracted intensities from crystals containing planar faults. *Proc. R. Soc. Lond. Ser. A* **433**, 499–520 (1991). doi:10.1098/rspa.1991.0062

29. S. Bette, R. E. Dinnebier, D. Freyer, Structure solution and refinement of stacking-faulted NiCl(OH). *J. Appl. Cryst.* **48**, 1706–1718 (2015). doi:10.1107/S1600576715017719

30. A. Kudielka, S. Bette, R. E. Dinnebier, M. Abeykoon, C. Pietzonka, B. Harbrecht, Variability of composition and structural disorder of nanocrystalline CoOOH

materials. *J. Mater. Chem. C Mater. Opt. Electron. Devices* **5**, 2899–2909 (2017). doi:10.1039/C6TC04626F

31. A. P. Hammersley, S. O. Svensson, M. Hanfland, A. N. Fitch, D. Hausermann, Two-dimensional detector software: From real detector to idealised image or two-theta scan. *High Press. Res.* **14**, 235–248 (1996). doi:10.1080/08957959608201408

32. P. Juhás, T. Davis, C. L. Farrow, S. J. L. Billinge, PDFgetX3: A rapid and highly automatable program for processing powder diffraction data into total scattering pair distribution functions. *J. Appl. Cryst.* **46**, 560–566 (2013). doi:10.1107/S0021889813005190

33. R. T. DeVol, R. A. Metzler, L. Kabalah-Amitai, B. Pokroy, Y. Politi, A. Gal, L. Addadi, S. Weiner, A. Fernandez-Martinez, R. Demichelis, J. D. Gale, J. Ihli, F. C. Meldrum, A. Z. Blonsky, C. E. Killian, C. B. Salling, A. T. Young, M. A. Marcus, A. Scholl, A. Doran, C. Jenkins, H. A. Bechtel, P. U. P. A. Gilbert, Oxygen spectroscopy and polarization-dependent imaging contrast (PIC)-mapping of calcium carbonate minerals and biominerals. *J. Phys. Chem. B* **118**, 8449–8457 (2014). doi:10.1021/jp503700g Medline

34. B. Ravel, M. Newville, ATHENA, ARTEMIS, HEPHAESTUS: Data analysis for X-ray absorption spectroscopy using IFEFFIT. *J. Synchrotron Radiat.* **12**, 537–541 (2005). doi:10.1107/S0909049505012719 Medline

35. U. Kolb, T. Gorelik, C. Kübel, M. T. Otten, D. Hubert, Towards automated diffraction tomography: Part I—data acquisition. *Ultramicroscopy* **107**, 507–513 (2007). doi:10.1016/j.ultramic.2006.10.007 Medline

36. E. Mugnaioli, T. Gorelik, U. Kolb, “Ab initio” structure solution from electron diffraction data obtained by a combination of automated diffraction tomography and precession technique. *Ultramicroscopy* **109**, 758–765 (2009). doi:10.1016/j.ultramic.2009.01.011 Medline

37. S. Schlitt, T. E. Gorelik, A. A. Stewart, E. Schömer, T. Raasch, U. Kolb, Application of clustering techniques to electron-diffraction data: Determination of unit-cell parameters. *Acta Crystallogr. A* **68**, 536–546 (2012). doi:10.1107/S0108767312026438 Medline

38. U. Kolb, T. Gorelik, M. T. Otten, Towards automated diffraction tomography. Part II—Cell parameter determination. *Ultramicroscopy* **108**, 763–772 (2008). doi:10.1016/j.ultramic.2007.12.002 Medline

39. M. C. Burla, R. Caliandro, B. Carrozzini, G. L. Cascarano, C. Cuocci, C. Giacovazzo, M. Mallamo, A. Mazzone, G. Polidori, Crystal structure determination and refinement via SIR2014. *J. Appl. Cryst.* **48**, 306–309 (2015). doi:10.1107/S1600576715001132

40. P. A. Doyle, P. S. Turner, Relativistic Hartree-Fock X-ray and electron scattering factors. *Acta Crystallogr. A* **24**, 390–397 (1968). doi:10.1107/S0567739468000756

41. G. M. Sheldrick, A short history of SHELX. *Acta Crystallogr. A* **64**, 112–122 (2008). doi:10.1107/S0108767307043930 Medline

42. U. Kolb, T. E. Gorelik, E. Mugnaioli, A. Stewart, Structural Characterization of Organics Using Manual and Automated Electron Diffraction. *Polym. Rev. (Phila. Pa.)* **50**, 385–409 (2010). doi:10.1080/15583724.2010.494238

43. I. P. Swainson, The structure of monohydrocalcite and the phase composition of the beachrock deposits of Lake Butler and Lake Fellmongery, South Australia. *Am. Mineral.* **93**, 1014–1018 (2008). doi:10.2138/am.2008.2825